Dual-Band CP Massive MIMO Antenna With Hybrid Absorber-AMC for Smart Mobility Systems

Asif Khan, *Member, IEEE*, Qingsha S. Cheng, *Senior Member, IEEE*, Muhammad Zada, *Member, IEEE*, Zhonghe Zhang, *Member, IEEE*, Yejun He, *Senior Member, IEEE*, and Qingfeng Zhang, *Senior Member, IEEE*

***Abstract*—Massive multiple-input multiple-output (mMIMO) antennas are crucial for enhancing channel capacity, link reliability, throughput, connectivity, beamforming, and efficiency in sub-6 GHz and beyond wireless communication. However, challenges such as mutual coupling (MC) and polarization mismatch must be addressed to ensure optimal performance. This article presents a 16-port dual-band circularly polarized mMIMO antenna intended for Wi-Fi and vehicle-to-everything (V2X) applications. The radiating element is a compact ($0.267\lambda_0 \times 0.267\lambda_0 \times 0.029\lambda_0$) square patch supporting dual resonance at 2.45 GHz (Wi-Fi IEEE 802.11n/g/ac) and 5.85 GHz [intelligent transportation systems (ITS)] via strategically placed slot perturbations. An array of a novel multifunctional modified labyrinthine absorber (MLA) incorporating discrete resistors and spiral inductors is introduced above the array to simultaneously suppress MC and effect linear-to-circular polarization conversion. In addition, a dual-band cross-grid artificial magnetic conductor (CGAMC) is deployed beneath the antenna array to enhance forward gain and preserve impedance matching. The prototype achieves measured −10 dB impedance bands of 2.40–2.50 and 5.50–6.00 GHz, axial-ratio (AR) ≤ 3 dB bandwidths of 100 and 370 MHz in the lower and upper bands, respectively, and measured peak realized gains of ≥ 5.23 dBi (2.45 GHz) and ≥ 5.83 dBi (5.85 GHz). Mean isolation across ports exceeds 22 dB, the envelope correlation coefficient (ECC) is less than 0.002, and total efficiency remains above 78% across both bands. The MLA is demonstrated to provide >90% absorptivity in the target bands while introducing an orthogonal phase shift that yields RHCP radiation; the CGAMC provides constructive reflection across both bands and increases forward directivity. Experimental measurements validate the simulation data with acceptable measurement uncertainty. The electromagnetic performance of the antenna is further assessed by mounting it on an open-source automotive model, where the rooftop of the car was tested with different materials, and it exhibits an omnidirectional radiation pattern.**

Received 11 April 2025; revised 11 October 2025; accepted 14 October 2025. Date of publication 30 October 2025; date of current version 21 January 2026. This work was supported in part by the National Natural Science Foundation of China under Grant 62071211, in part by Shenzhen Science and Technology Program under Grant JCYJ20240813095713018, and in part by the National Key Research and Development Program of China under Grant 2023YFE0107900. *(Corresponding author: Qingsha S. Cheng.)*

Asif Khan, Qingsha S. Cheng, and Qingfeng Zhang are with the Department of Electronic and Electrical Engineering, Southern University of Science and Technology, Shenzhen 518055, China (e-mail: asifm20019@gmail.com; chengqs@sustech.edu.cn; zhangqf@sustech.edu.cn).

Muhammad Zada is with the Department of Health Sciences and Technology, ETH Zürich, 8092 Zürich, Switzerland (e-mail: muhammad.zada@hest.ethz.ch).

Zhonghe Zhang and Yejun He are with the College of Electronics and Information Engineering, Shenzhen University, Shenzhen 518060, China (e-mail: 422384683@qq.com; heyejun@126.com).

Digital Object Identifier 10.1109/TAP.2025.3625287

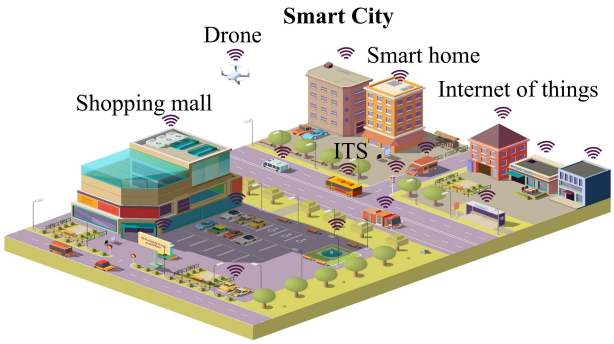

Fig. 1. Application scenario of the proposed mMIMO antenna for ITS communication in a smart city.

***Index Terms*—Cross-grid artificial magnetic conductor (CGAMC), massive multiple-input multiple-output (mMIMO), modified labyrinthine absorber (MLA), smart mobility, spatial diversity.**

I. Introduction

THE rapid expansion of data-driven services, increased user mobility, and the deployment of smart technologies have driven a growing demand for wireless communication systems that offer high capacity, low latency, and broad coverage. However, the performance of such systems is critically limited by the efficiency and robustness of the antenna subsystems, particularly in dynamic and multipath-rich environments. To meet these requirements, multiantenna technologies such as antenna arrays, multiple-input multiple-output (MIMO) antennas, and massive MIMO (mMIMO) antenna systems have become central to modern wireless infrastructure. These architectures enable spatial multiplexing and diversity, thus improving spectral efficiency and communication robustness [1], [2]. Consequently, multi-antenna systems are increasingly implemented across a variety of practical platforms, including smart homes, industrial automation, stadiums, base stations, and intelligent transportation systems (ITS), as illustrated in the system-level scenario in Fig. 1 Among the key technological pillars of ITS are the Internet of Vehicles (IoV), which facilitate real-time data exchange among vehicles, infrastructure, and pedestrians through vehicle-to-everything (V2X) communication technologies [3]. This capability is vital for enabling connected autonomous vehicles, intelligent traffic control, and advanced driver assistance systems. To support

these applications, the 2.4 and 5.8 GHz bands are commonly adopted due to their compatibility with Wi-Fi and dedicated short-range communication (DSRC) [4], [5], making them ideal for vehicular networks requiring both Internet of Things (IoT)-based monitoring and high-speed data links.

To ensure robust and reliable V2X communication under high mobility and multipath conditions, antenna systems must support dual-band operation, maintain polarization diversity, and exhibit compact size and low cost. In this context, CP antennas are highly desirable because they minimize polarization mismatch, enhance immunity to multipath fading, and allow orientation-independent signal reception. These characteristics are particularly valuable in mobile environments, such as vehicles. The integration of CP antennas into mMIMO configurations further enhances channel capacity, spectral efficiency, and overall system reliability.

Despite these benefits, designing compact dual-band CP mMIMO antennas for vehicular platforms remains a significant challenge. Achieving simultaneous CP at multiple frequencies requires careful mode excitation and current distribution optimization while maintaining low mutual coupling (MC) and a compact form factor. These design trade-offs are complicated to manage in vehicular platforms, where physical space and integration complexity are critical constraints.

Numerous studies have been conducted on dual-band MIMO antennas to address isolation and bandwidth limitations [6], [7], [8], [9], [10], [11]. For instance, [6] employed back-to-back planar inverted-F antennas with an isolation-enhancing decoupling structure, while [7] utilized a resonant branch and T-shaped slot to enhance separation between dual-band inverted-F antenna elements. More advanced techniques include the use of metasurfaces (MSs) and defected ground structures to suppress coupling in closely spaced MIMO antennas [8], [12]. Alternatively, electromagnetic band gap structures with MS lenses [9] and a modified Jerusalem cross absorber (MJCA) [25] have been used to improve isolation in MIMO antennas. However, most of these systems are limited to linear polarization (LP), which is prone to performance degradation due to polarization mismatch in mobile environments.

To address these challenges, various LP-to-CP conversion techniques were investigated. For single-band systems, MSs were used for effective LP-to-CP conversion [13] at 2.45 GHz, while [14] shows how broadband MS can achieve polarization conversion with sidelobe suppression through independent amplitude/phase control. However, these single-band solutions often require multi-layer structures and complex feeding networks, increasing antenna profile and size in wideband operation [15]. For multiband applications, several designs have been proposed, including Jerusalem cross radiators [16], hybrid C- and I-type patches with embedded stubs [17], and folded JC patches [23]. Other approaches include dual-band split-ring resonators with stubs [18] and ring-based CP metastructures [19]. While these methods achieve dual-band CP, they typically require additional feed-to-conversion distances, leading to increased antenna complexity. Alternative multi-band solutions employing chiral metamaterials and shared-aperture transmit arrays were also investigated [20], [21]. Similarly, dual-band CP is achieved through cuts and perturbation [25]. The work in [22] presents a dual-band implementation but is limited to a single antenna element.

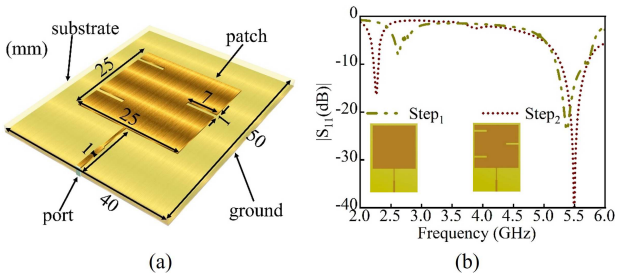

Fig. 2. Illustration of the design process (a) single antenna and (b) S_{11} of the iterative steps.

Moreover, recent developments in compact CP antennas using metamaterials, artificial magnetic conductors (AMCs), and absorbers have shown potential in improving gain and isolation [24], [25]. CP designs based on circular patches with shorting pins or spiral arms offer compact profiles [26], [27], while dielectric resonator antennas provide wide bandwidths and low loss [28], though at the cost of larger volume. Despite these efforts, many existing dual-band CP MIMO antennas either operate with narrow bandwidths, lack true dual-band CP behavior, or fail to support the entire range of ISM/unlicensed bands required for IoV applications [29], [30], [31], [32]. Despite the extensive literature, most prior works focus solely on either single-band operation, isolation enhancement, polarization conversion, or gain improvement. A multifunctional antenna that simultaneously addresses dual-band operation, CP, high gain, and strong isolation in a compact mMIMO configuration remains underexplored.

To address these limitations, this work proposes a compact 16-port dual-band circularly polarized mMIMO antenna optimized for V2X and Wi-Fi applications. The antenna operates at two key frequency bands, 2.4–2.5 and 5.5–6 GHz, while maintaining a compact design despite its 16-port configuration. A novel multifunctional dual-band MLA is introduced that incorporates lumped components, marking the first absorber capable of achieving dual-band absorptivity exceeding 90% in both frequency bands through optimized resistors and inductors, thus reducing MC. Beyond its absorption property, the MLA also functions as a polarizer, effectively converting linearly polarized waves to circular, a dual functionality not previously demonstrated in existing absorbers. Incorporating a dual-band cross-grid artificial magnetic conductor (CGAMC) serves to enhance gain, improve isolation, and optimize the antenna's overall performance.

II. Antenna Design

A. Single Antenna

The geometric design and structural details of the proposed microstrip antenna are illustrated in Fig. 2(a). The antenna features three rectangular slots in the patch mounted on an FR4 substrate. A 50 Ω microstrip feed line is employed to excite the antenna. The overall dimensions of the antenna are

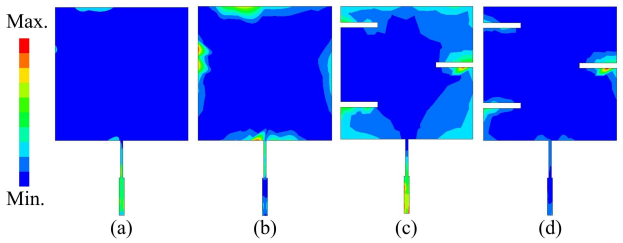

Fig. 3. Surface current distribution of the simple patch antenna at (a) 2.25 and (b) 5.5 GHz, and of the proposed antenna at (c) 2.25 and (d) 5.5 GHz.

$0.267\lambda_0 \times 0.267\lambda_0 \times 0.029\lambda_0$ at 2.4 GHz. Fig. 2(b) shows that the simple patch antenna initially resonated at 5.4 GHz. The incorporation of three rectangular slots, which modify the resonance characteristics of the patch and enable dual-frequency operation, allows the antenna to resonate at 2.2–2.3 and 5.5–5.75 GHz.

The surface current distributions of the proposed single antenna at the operating frequencies of 2.25 and 5.5 GHz, with and without slots, are depicted in Fig. 3. The surface current intensity at 2.25 GHz is almost negligible, as shown in Fig. 3(a). At 5.5 GHz, as shown in Fig. 3(b), the current intensity is significantly higher without slots, which results in a reflection coefficient of less than −30 dB, as previously discussed in Fig. 2.

To achieve an additional resonance at the lower band, three slots were incorporated into the patch at locations where the surface current is strongest. These slots extend the current path and activate a larger portion of the patch, enabling resonance at the lower frequency, as illustrated in Fig. 3(c). At 5.5 GHz, the effect of the slots is minimal, and the current distribution remains nearly unchanged, as shown in Fig. 3(d). Based on the above analysis, the introduced slots not only extend the current path but also create an additional one. Consequently, the patch supports two distinct current paths: an extended path responsible for the lower frequency (2.25 GHz) and a shorter path for the higher frequency (5.5 GHz).

B. Modified Labyrinthine Absorber

1) Initial Design: The proposed MLA is derived from an MJCA [25], as shown in Fig. 4(a). Rogers 5880 is employed as a substrate, and the unit cell dimensions are $0.458\lambda_0 \times 0.458\lambda_0 \times 0.032\lambda_0$. Originally designed for operation in the 6.5–8.5 GHz range, the structure was optimized to achieve dual-band operation at 2.4 and 5.85 GHz. To lower the operating frequencies and enhance performance, external branches were added to the MJCA, which effectively extended the current path and shifted the resonance to lower frequencies. In addition, four spiral-shaped inductors (2.5 nH each) were integrated into the inner segments of the labyrinthine structure. These inductors further extend the current path, improve impedance matching, and stabilize the resonance. The final design achieves an absorptivity of 90% and a reflectivity of ≤−10 dB across the target bands, as shown in Fig. 4(b).

A parametric study was conducted to evaluate three key design modifications. First, the addition of external branches

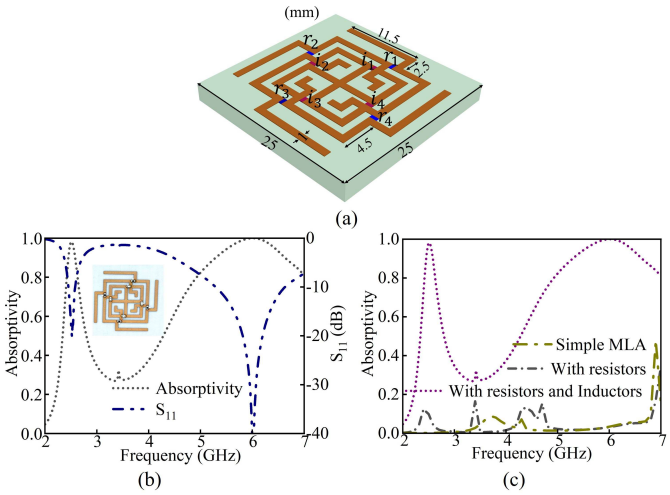

Fig. 4. Analysis of the absorber design and performance (a) MLA, (b) S_{11} and absorptivity, and (c) absorptivity of the iterative steps.

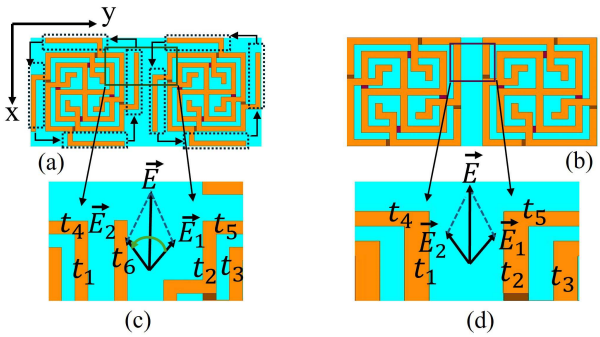

Fig. 5. Topology of MLA array (a) proposed MLA with extra branches, (b) without extra branches, (c) zoomed-in view part with branches, and (d) conventional absorber without extra branches.

alone was analyzed, which resulted in an absorptivity of only 2% across the spectrum, as shown in Fig. 4(c), and was insufficient for an effective absorber. Next, four resistors (160 Ω each) were incorporated, which extended the current path and introduced resonance peaks at 3.2 and 4.5 GHz. However, absorptivity remained limited to 10%–15%. Finally, four inductors (2.5 nH each) were added to the inner branches. Together with the external branches, these inductors further extended the current path, which led to a significant improvement in absorption performance. The optimized structure, integrating external branches, inductors, and resistors, achieved absorption exceeding 90% in the 2.4–2.5 and 5.5–6 GHz bands, as shown in Fig. 3(c).

2) Equivalent Circuit Model: As discussed earlier, the proposed MLA not only reduces MC but also functions as a polarizer. The improvement in circular polarization is attributed to the asymmetric labyrinthine geometry and the inductor-induced phase shift, which redistribute surface currents and promote orthogonal field components.

Equivalent circuits are employed to explain how the proposed MLA structure converts LP to CP waves. The RH-MLA shown in Fig. 5(a) is used in the proposed antenna for this purpose. The MLA is redrawn in Fig. 5(c), where the enclosed pattern is treated as a new unit cell. For clarity, the enlarged unit cell is illustrated in Fig. 5(c) with strips labeled

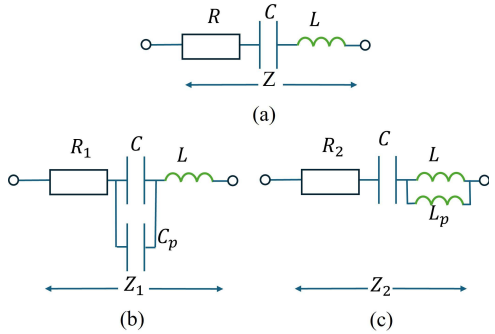

Fig. 6. Equivalent circuits of (a) unit cell with strip t_6 removed seen by $\vec{E}_1$ and $\vec{E}_2$, (b) proposed unit cell seen by $\vec{E}_1$, and (c) $\vec{E}_2$ with t_6, respectively.

t_1, t_2, t_3, t_4, t_5, and t_6. Fig. 5(d) shows the same unit cell with the strip t_6 removed.

When the RH-MLA in Fig. 5(a) is positioned near the mMIMO antenna generating an LP signal, an electric field (E) develops along the X-axis, as shown in Fig. 5(c). This field can be decomposed into two orthogonal components, E_1 and E_2. If the strip t_6 is removed, as shown in Fig. 5(d), the E_1 component experiences the unit cell as an RLC circuit, represented in Fig. 6(a), with impedance given by [13]

$$Z = R + j\left(\omega L - \frac{1}{\omega C}\right). \tag{1}$$

Here, C represents the capacitance formed by the electric fields across the gaps between strip pairs (t_1, t_2) and (t_4, t_5), L is the inductance due to currents on the strips, and R is the resistance of the strips. Owing to symmetry, the $\vec{E}_2$ component also experiences the same impedance.

When t_6 is included in the unit cell, as shown in Fig. 5(c), the impedances Z_1 and Z_2 experienced by $\vec{E}_1$ and $\vec{E}_2$, respectively, are modified. For $\vec{E}_1$, the electric fields on t_6 create an additional capacitance (C_p), which is in parallel with C, forming the equivalent circuit in Fig. 6(b). The combined capacitance ($C \parallel C_p$) is less than C, making $\vec{E}_1$ less capacitive than Z.

For $\vec{E}_2$, the currents on the strip t_6 generate additional inductance (L_p), which is in parallel with L, as shown in Fig. 6(c). The resultant inductance ($L \parallel L_p$) is less than L, making Z_2 less inductive than Z.

Since Z_1 is less capacitive than Z and Z_2 is less inductive than Z, a phase difference of $\arg(Z_1 - Z_2)$ is introduced between E_1 and E_2 as the wave passes through the MS. The impedances Z_1 and Z_2 can be expressed as [13]

$$Z_1 = R_1 + j\left(\omega L - \frac{1}{\omega\left(C \parallel C_p\right)}\right) \tag{2}$$

$$Z_2 = R_2 + j\left(\omega\left(L \parallel L_p\right) - \frac{1}{\omega C}\right). \tag{3}$$

The presence of the strip t_6 thus controls the phase difference between Z_1 and Z_2. When the conditions $|Z_1| = |Z_2|$ and $\angle Z_1 - \angle Z_2 = 90^\circ$ are satisfied, $|E_1| = |E_2|$ and $\angle E_1 - \angle E_2 = 90^\circ$. In this scenario, E_2 leads E_1 by 90°, resulting in an RHCP electric field through the MLA structure.

TABLE I
COMPARISON OF MJCA [25] AND PROPOSED MLA

Ref.	MJCA [25]	Proposed MLA
Core structure	Based on resistors only	Based on resistors and inductors
Primary function	Absorptivity	Absorptivity and polarization conversion
Absorptivity band	A single wideband	Two distinct bands
Isolation enhancement (dB)	12	10
AR bandwidth (%)	None	4.08, 6.43
Gain enhancement (dBi)	2, 3.5	7, 7

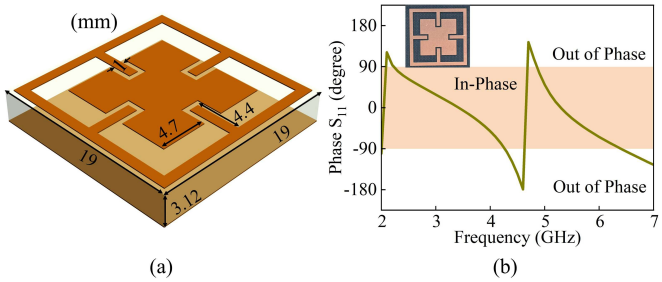

Fig. 7. Visualization of the proposed CGAMC (a) schematic view and (b) reflection phase response.

Similarly, as observed in Fig. 5(a), the L-shaped strips (t_6, one of them), highlighted by dotted rectangles, are oriented to align with the current in the right-hand direction. This confirms that MLA converts LP into RHCP.

A quantitative comparison between the MJCA [25] and the proposed MLA when integrated with the mMIMO antenna is presented in Table I. The MJCA pattern [25] is based on resistors, functioning only as an absorber. In contrast, the proposed MLA features a labyrinthine structure with external branches that integrates both resistors and inductors, enabling simultaneous absorption and polarization conversion across two distinct bands. The proposed design demonstrates notable improvements, including higher realized gain, wider AR bandwidth, and enhanced isolation.

C. CGAMC Design

The CGAMC unit cell features a novel symmetric cross-shaped structure with an integrated cross-grid pattern, as shown in Fig. 7(a). The design consists of an outer square ring with four stubs and an inner square patch etched with four rectangular slots. The unit cell is printed on a $0.235\lambda_0 \times 0.235\lambda_0 \times 0.039\lambda_0$ Taconic TLY substrate with a relative permittivity of 2.2 and a loss tangent of 0.0009.

The dual-band functionality of the unit cell is achieved through a parametric study of its geometry. The outer square ring with four stubs acts as a resonator at the lower frequency band around 2.4 GHz, with the stubs enhancing capacitive and inductive coupling to achieve the desired resonance. Meanwhile, the inner square patch etched with four rectangular slots resonates in the higher frequency band around 5.85 GHz. The slots modify the current distribution and create additional

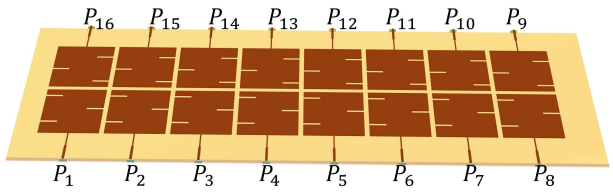

Fig. 8. Simulated model of the initial 16-port mMIMO antenna.

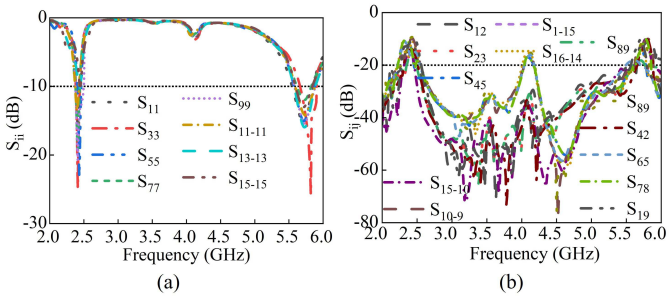

Fig. 9. S-parameters of the simple mMIMO antenna (a) S_{ii} and (b) S_{ij}.

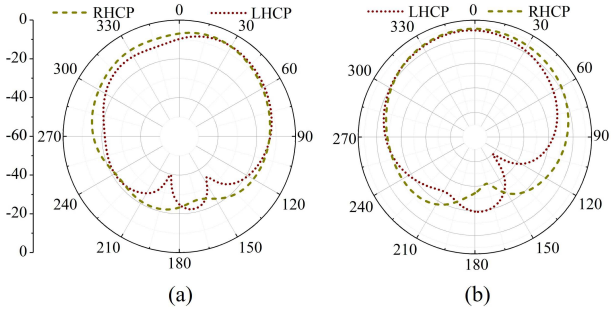

Fig. 10. Radiation patterns of the initial mMIMO antenna at (a) 2.45 and (b) 5.85 GHz.

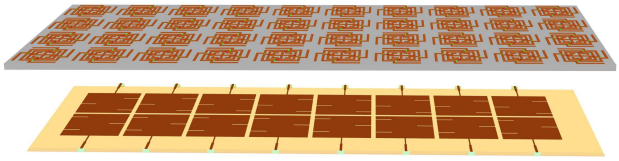

Fig. 11. Configured mMIMO antenna integration with MLA.

resonant paths, while the rectangular stubs extending into the slots further contribute to the coupling between the outer ring and the inner patch, ensuring stable dual-band behavior. The reflection phase response exhibits two wide $\pm 90°$ reflection phase bandwidths: 2.3–5.4 and 5.6–7 GHz, as shown in Fig. 7(b).

III. Massive MIMO Antenna Integration

This section describes the development of the 16-port mMIMO antenna and its integration with the MLA and CGAMC. Section III-A discusses the design of the baseline mMIMO antenna and its S-parameters. Section III-B examines the impact of the MLA on MC, radiation patterns, and polarization conversion. Section III-C presents the integration of the CGAMC layer, focusing on its role in enhancing gain, improving isolation, and influencing CP performance. Finally, the combined performance of MLA and CGAMC is evaluated, highlighting isolation enhancement, gain improvements due to the CGAMC versus degradation caused by the MLA, AR improvement achieved with the MLA versus its degradation by the CGAMC, and the overall effect are presented in Section III-D.

A. Initial mMIMO Antenna

The proposed mMIMO antenna consists of two symmetrical rows of eight elements each, with an element-to-element spacing of $0.03\lambda_0$, as shown in Fig. 8. The single antenna originally operated in the 2.2–2.3 GHz range. However, when integrated into the mMIMO configuration, the operating frequency shifted upward to 2.4–2.5 GHz. This shift occurred due to MC, which slightly perturbed the resonance. A similar effect was observed in the upper band, where the original resonance at approximately 5.5 GHz shifted to around 5.7 GHz.

Fig. 9 presents the S-parameters of the mMIMO antenna, including the reflection coefficients (S_{ii}) and coupling parameters (S_{ij}). In Fig. 9(a), the reflection coefficients (S_{11}, S_{33}, S_{55}, S_{77}, S_{99}, etc.) indicate that the antenna operates over two distinct frequency bands: a narrow resonance from 2.4 to 2.5 GHz and a wider band from 5.5 to 6 GHz.

Since the antenna elements are placed in close proximity, strong coupling occurs across both bands, as shown in Fig. 9(b). MC arises when electromagnetic fields radiated by one element induce currents or fields in adjacent elements. This interaction occurs through space waves, surface waves, or currents on the common ground plane. The coupling between P_1 and P_2 is approximately −7 dB, while the coupling between P_1 and P_3, P_1 and P_5, and P_1 and P_7 is approximately $\geq$ −11 dB. These levels are above the conventional isolation threshold of −15 dB. However, MC also contributes to bandwidth enhancement. As shown in Fig. 9(a), the mMIMO antenna achieves a 500 MHz bandwidth in the upper band, compared to the 275 MHz bandwidth of a single antenna in Fig. 2(a). This increase arises because coupling alters the effective impedance of each element, thereby broadening the overall impedance bandwidth. Specifically, interaction between adjacent elements introduces new resonances and shifts existing resonant modes, further extending the bandwidth.

Fig. 10 illustrates the polarization characteristics through the radiation pattern. When the RHCP and LHCP components have equal magnitude, the antenna exhibits LP. In the initial design, this balance is observed, confirming that the array does not generate a dominant CP component at either 2.45 or 5.85 GHz, as shown in Fig. 10(a) and (b).

B. Integration With MLA Array

An array of 13 × 5 MLA elements was integrated into the mMIMO antenna at a height of 4 mm, as shown in Fig. 11. The height was determined through parametric optimization.

The primary function of the MLA layer is to enhance isolation in mMIMO antennas by mitigating MC between closely spaced elements. MC from surface currents and stray radiation increases port correlation and reduces diversity and multiplexing gain.

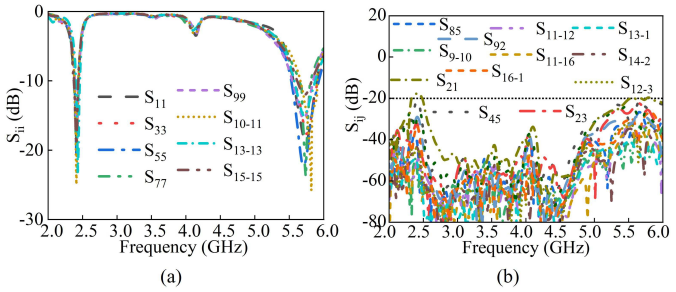

Fig. 12. Performance analysis of the proposed mMIMO antenna with the MLA (a) S_{ii} and (b) S_{ij}.

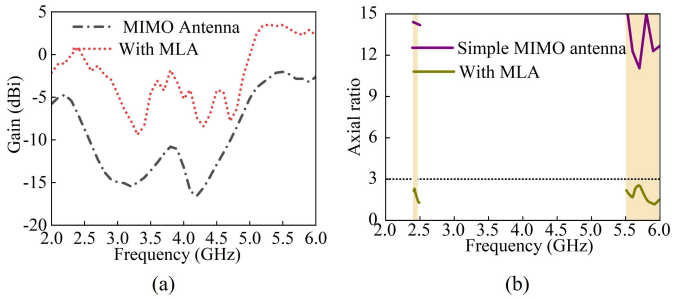

Fig. 13. mMIMO antenna incorporates the proposed MLA (a) AR and (b) Gain.

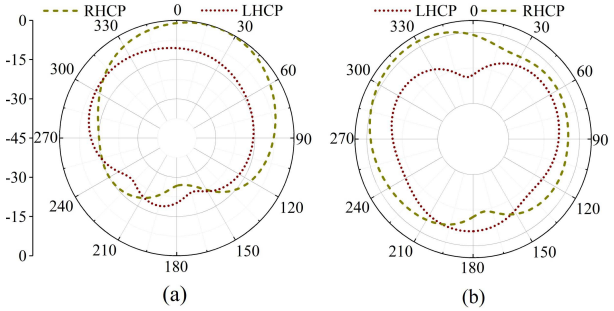

Fig. 14. LHCP and RHCP radiation patterns of the mMIMO antenna with MLA at (a) 2.45 and (b) 5.85 GHz.

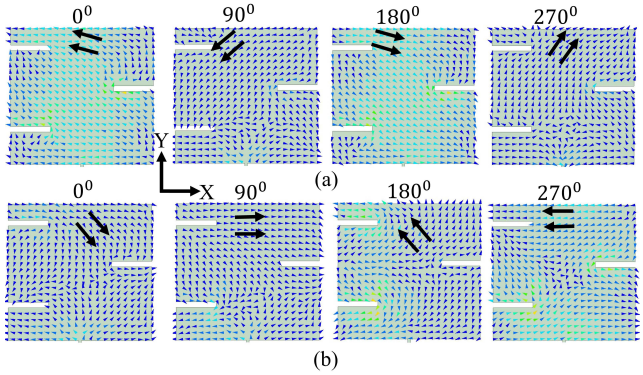

Fig. 15. Surface current distribution of the mMIMO antenna design at different angles with the MLA layer only (a) at 2.45 and (b) 5.85 GHz.

The MLA slightly affects the reflection coefficient (S_{ii}), but the overall impact is negligible, and the antenna continues to resonate in the desired bands. The achieved bandwidths are 100 MHz from 2.4 to 2.5 GHz in the lower band and 500 MHz from 5.5 to 6 GHz in the upper band, as illustrated in Fig. 12(a).

The MLA layer, positioned above the antenna, absorbs unwanted coupled radiation between elements. With an absorptivity exceeding 90% in both operating bands, most of the interfering currents and radiated electromagnetic energy are absorbed before reaching the neighboring elements. This suppression of surface waves and radiated fields effectively reduces MC, improving isolation by up to 10 dB (from 11 to 21 dB) across the frequency bands, as shown in Fig. 12(b).

Fig. 13(a) shows the realized gain of the proposed 16-port mMIMO antenna with the MLA. The gain increases from −6.5 to 0.5 dBi in the lower band and from −2.5 to 3.5 dBi in the upper band. The improvement arises from the suppression of surface waves and higher-order modes, as well as the mitigation of backward radiation. In the MLA layer, resistive components dissipate unwanted surface currents, while inductive elements control phase and amplitude, improving impedance matching. This directs more power forward, enhancing directivity and realized gain despite the MLA's inherent losses.

Fig. 13(b) shows the AR $\leq$ 3 dB bandwidths for both operating bands, achieving 100 and 500 MHz, respectively. In addition to improving isolation, the MLA facilitates polarization conversion, transforming LP into CP. This is achieved through its anisotropic geometry, which reshapes surface currents and manipulates electromagnetic fields. The structure introduces a phase difference 90° between the components of the orthogonal wave, a key requirement of CP.

To further confirm the polarization conversion capability, the LHCP and RHCP radiation patterns of the proposed mMIMO antenna are illustrated in Fig. 14. When the MLA layer is added, the antenna's polarization shifts from LP to CP, maintaining well-structured radiation patterns with minimal distortion. In the baseline mMIMO antenna (Fig. 10), the LHCP and RHCP components are identical. In contrast, Fig. 14 shows that RHCP is 10 dB stronger than LHCP, which confirms CP operation. At 2.45 GHz, RHCP dominates from 0° to 60°, as shown in Fig. 14(a). Similarly, at 5.85 GHz, RHCP dominates from 315° to 0°, as shown in Fig. 14(b).In general, an ideal CP is realized by two orthogonal electric field vectors possessing equal amplitudes and a phase difference of 90°. This condition is achieved when the amplitudes of the two orthogonal currents are equal and their phase difference is 90°, resulting in an ideal current distribution. To illustrate the mechanism of CP implementation, Fig. 15 presents the surface current distribution of the MLA-based mMIMO antenna, viewed from the +Z-axis, at four distinct phases (0°, 90°, 180°, and 270°) at 2.45 and 5.85 GHz.

Fig. 15(a) displays the current distribution of the mMIMO antenna at 2.45 GHz. At the 0° phase, the direction of the synthesized current is primarily along the −X-axis. At the 90° phase, the direction of the generated current is mainly along the −Y-axis. At the 180° phase, the direction of the synthesized current is primarily oriented along the X-direction. At the 270°

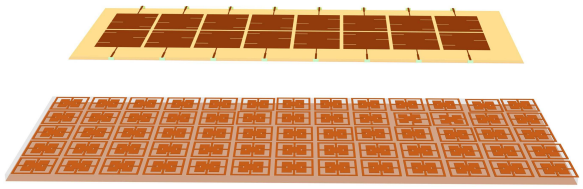

Fig. 16. Simulated model of the mMIMO antenna configuration with the CGAMC layer only.

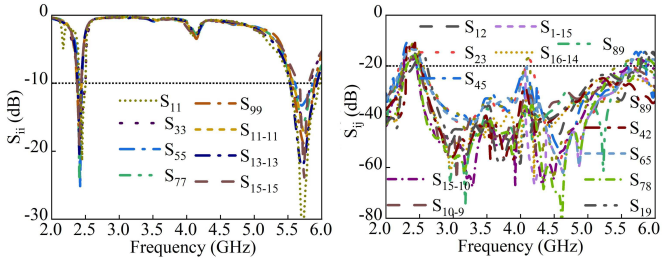

Fig. 17. Impact of the CGAMC on (a) S_{ii} and (b) S_{ij}.

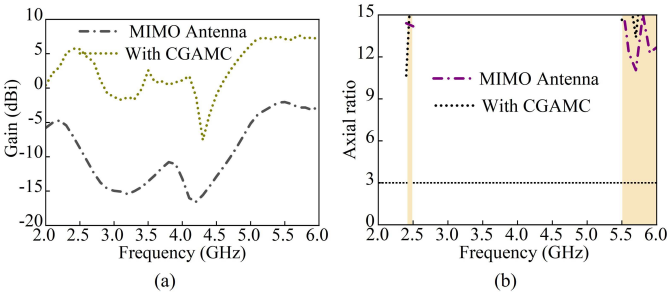

Fig. 18. CGAMC array's influence on (a) gain improvement and (b) AR performance of the mMIMO antenna.

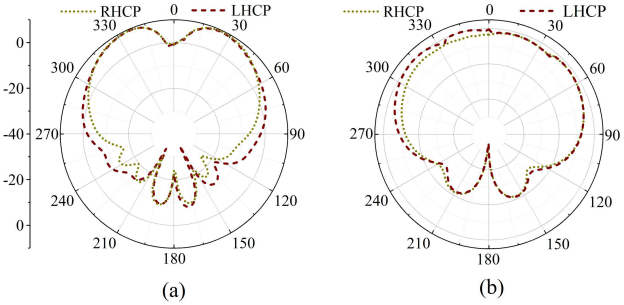

Fig. 19. Radiation performance based on the CGAMC layer in terms of LHCP and RHCP at (a) 2.45 and (b) 5.85 GHz.

phase, the direction of the synthesized current is predominantly along the Y-direction. For the two pairs of phases, 0° and 180° as well as 90° and 270°, the amplitude of the current remains equal, but the directions are opposite. As the current rotates counterclockwise, the antenna generates RHCP wave radiation at a frequency of 2.45 GHz. Similarly, Fig. 15(b) shows the surface current distribution at different phases at 5.85 GHz. At 0°, the surface current of the antenna is synthesized in the $-Y$-direction. At the 90° phase, it is directed along the X-axis. At the 180° and 270° phases, the surface current possesses the same magnitude but is in the opposite direction with respect to that at the 0° and 90° phases, respectively. Therefore, the RHCP characteristics are realized at 5.85 GHz.

C. Integration With Cross-Grid AMC

To examine the effect of the CGAMC layer on the antenna performance, Fig. 16 illustrates its integration with the mMIMO antenna. A 5 × 12 array of CGAMC elements was positioned beneath the mMIMO antenna at an optimized height of 14 mm, determined through parametric studies.

Fig. 17 presents the simulated S-parameters of the proposed antenna with the CGAMC. Fig. 17(a) shows the reflection coefficient, which indicates that the antenna maintains its operating bands of 2.4–2.5 and 5.5–6.0 GHz with minimal frequency shift. Since the CGAMC primarily enhances isolation and gain, its impact on the input impedance is negligible. Fig. 17(b) shows the MC between elements. In the lower band, isolation improves from 11 to 14 dB, while in the upper band, it improves from 11 to 16 dB, confirming a reduction in coupling. The improvement arises from the suppression of surface-wave propagation by the CGAMC.

Fig. 18 illustrates the effect of the CGAMC on the gain and AR performance of the mMIMO antenna. Substantial gain improvement is achieved due to the reflective properties of the CGAMC and its wide ±90° reflection-phase bandwidth, which spans both operating bands of the antenna. With larger lateral dimensions (100 × 260 mm) than the antenna array, the CGAMC captures backward radiation and redirects it in phase, suppressing destructive interference and reinforcing forward radiation. This constructive reflection increases the realized gain, as shown in Fig. 18(a). Specifically, the gain rises from –6.5 to 5.7 dBi in the lower band (improvement of 12.2 dB) and from –2.5 to 8.5 dBi in the upper band (improvement of 11 dB). Meanwhile, Fig. 18(b) evaluates the influence of the CGAMC on AR, where noticeable fluctuations appear in both bands. AR decreases from 15 to 13 dB, while in the upper band, AR increases from 12 to 14 dB. These fluctuations arise from the periodic structure of the CGAMC and its interaction with surface currents. However, the overall impact on CP is minimal.

Furthermore, Fig. 19 presents the LHCP and RHCP radiation patterns of the antenna integrated with the CGAMC at 2.45 and 5.85 GHz. Compared to the reference mMIMO case in Fig. 10, a slight angular deviation of the main lobe is observed, particularly in the lower band. Quantitative analysis of the far-field patterns shows that at 2.45 GHz, the main lobe is tilted by approximately 7° in the RHCP (E-plane) and the LHCP (H-plane), while at 5.85 GHz, there is no tilt. This confirms that the distortion is minor and does not compromise radiation coverage.

The impact of the CGAMC layer on the proposed MIMO antenna is further analyzed through the surface current distribution shown in Fig. 20. At 2.4 GHz, the major current flows along the X-axis at all phase states, indicating an LP characteristic, as illustrated in Fig. 20(a). A similar trend is

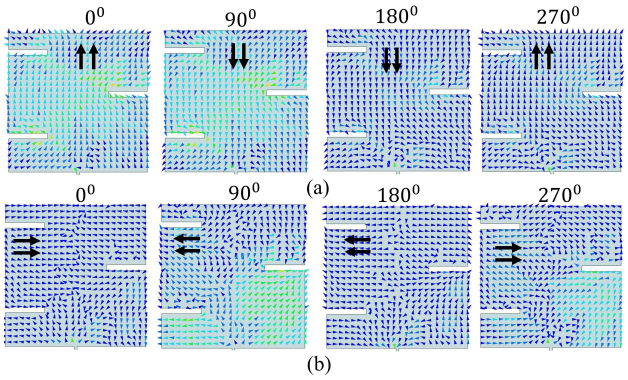

Fig. 20. Surface current distribution of CP antenna design at different angles based on CGAMC layer only (a) at 2.45 and (b) 5.85 GHz.

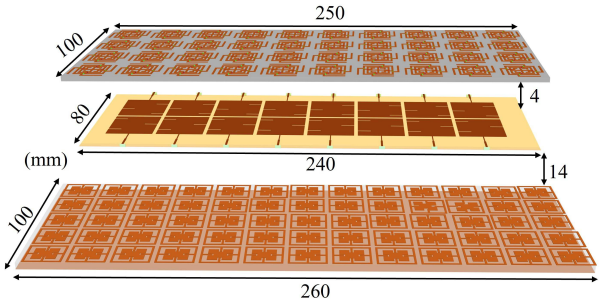

Fig. 21. Simulated model of the three-layer mMIMO antenna configuration, including the MLA and CGAMC layers.

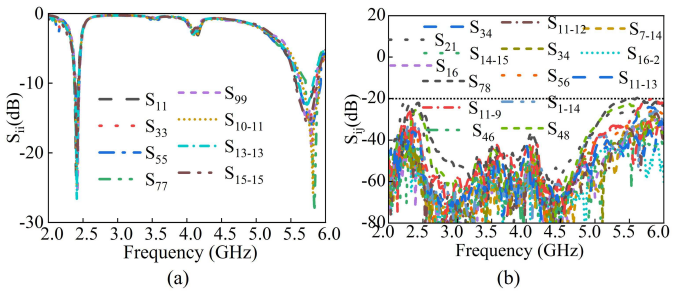

Fig. 22. Evaluation of the final mMIMO antenna (a) S_{ii} and (b) S_{ij}.

observed at 5.85 GHz, where the dominant current flows along the Y-axis, as shown in Fig. 20(b).

D. Performance Analysis of mMIMO Antenna Enhanced by MLA and CGAMC Structures

The final configuration of the proposed mMIMO antenna is shown in Fig. 21. The system comprises three stacked layers: the MLA array on top, the 16-port MIMO antenna in the middle, and the CGAMC at the bottom.

As shown in Fig. 22(a), the reflection coefficients (S_{ii}) remain similar to those in Fig. 9(a), confirming that the impedance matching is largely unaffected. Fig. 22(b) demonstrates an improvement in isolation, where S_{ij} increases by approximately 3 dB across both bands, reaching 22 and 25 dB compared to the 20 dB baseline. This confirms that the

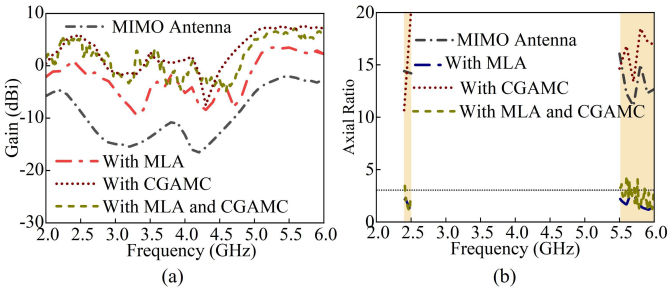

Fig. 23. Proposed mMIMO antenna when integrating with MLA and CGAMC in terms of (a) Gain and (b) AR.

combined layers effectively suppress surface waves and reduce MC among the ports.

Fig. 23(a) illustrates the realized gain performance, where the initial mMIMO antenna exhibits low gains of −6.5 and −2.5 dBi in the lower and upper bands, respectively, due to its small electrical size at 2.45 GHz ($0.267\lambda_0 \times 0.267\lambda_0 \times 0.029\lambda_0$). Integration of the MLA primarily suppresses MC and surface waves, resulting in improved radiated power. The gain increases to 0.5 dBi in the lower band and 3.5 dBi in the upper band, corresponding to improvements of 7.0 and 6.0 dB, respectively.

When only the CGAMC layer is included, a more substantial gain enhancement is observed. The gain rises from −6.5 to 5.7 dBi in the lower band and from −2.5 to 8.5 dBi in the upper band. This enhancement results from the CGAMC's reflective mechanism, which redistributes surface currents and reinforces forward radiation through constructive interference.

When both MLA and CGAMC are integrated, the gain in the lower band stabilizes at approximately 5.23 dBi. In contrast, the gain in the upper band decreases slightly from 8.5 dBi (CGAMC only) to 6.0 dBi. This reduction is attributed to the lossy components of the MLA, which absorb part of the radiated energy that the CGAMC would otherwise redirect. However, the impact is limited since the lumped components are positioned away from the main radiating regions, which minimizes performance degradation.

Furthermore, the impact of both layers on AR performance was illustrated in Fig. 23(b). While AR remains below 3 dB across the entire lower band, fluctuations are observed in the upper band, with values occasionally approaching the 3 dB threshold. Despite these variations, the AR < 3 dB bandwidth in the upper band spans 370 MHz, covering 5.5–5.6, 5.7–5.8, and 5.83–6.0 GHz. These fluctuations arise from stronger coupling and higher-order resonances introduced by the periodic CGAMC structure, which perturb the phase balance required for stable CP.

The introduction of both CGAMC and MLA layers modifies the radiation patterns, as shown in Fig. 24(a) and (b). Although CGAMC alone slightly tilts the main lobe under LP, adding MLA accentuates this effect in the side lobes and enhances beam formation around 0°. The MLA converts polarization from linear to circular, and the reflected waves from the CGAMC interact with the altered phase fronts, causing minor sidelobe distortions due to phase mismatch and coupling.

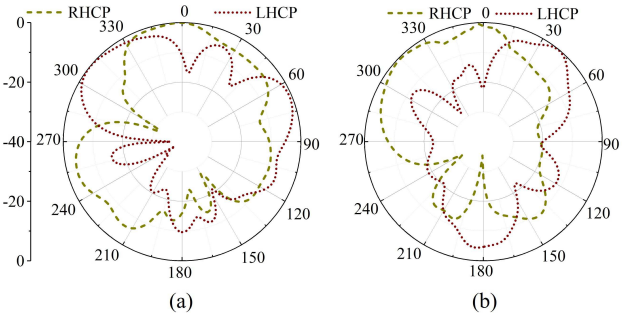

Fig. 24. Radiation patterns when integrated with the MLA and CGAMC layer at (a) 2.45 and (b) 5.85 GHz.

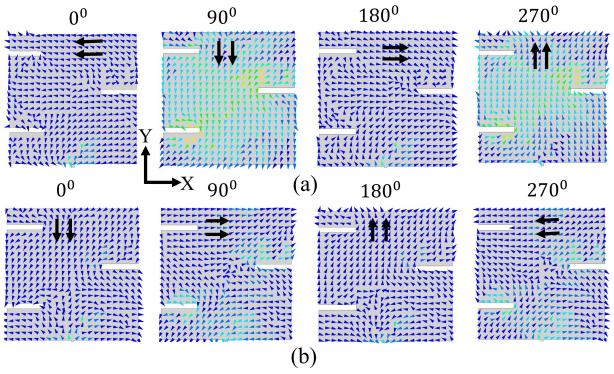

Fig. 25. Surface current distributions of the final CP mMIMO antenna design incorporating the CGAMC and MLA layers at different angles (a) at 2.45 and (b) 5.85 GHz.

However, the antenna maintains stable RHCP performance. At 2.45 GHz, RHCP dominates the broadside region near 0°, while at 5.85 GHz, it remains dominant over the 300°–0° angular range.

The surface current distributions of the final mMIMO antenna with all integrated layers are analyzed at multiple phase instants, as shown in Fig. 25. With the inclusion of the MLA layer, as discussed in Fig. 15, the currents flow symmetrically along different phases, consistent with stable CP. When the CGAMC layer is added, slight deviations appear at all phase instants compared to Fig. 15. However, the overall current flow remains aligned within the designed phases for the lower band, as illustrated in Fig. 25(a). Similarly, for the upper band, minor deviations occur at 0° and 180°, as shown in Fig. 25(b). This indicates that the CGAMC layer introduces only marginal asymmetry in the current distribution, and the polarization remains stable, with RHCP dominating both bands.

E. Measured Results

To validate the simulated performance, the proposed antenna was optimized using ANSYS HFSS and subsequently fabricated, as shown in Fig. 26.

Experimental validation was performed using the same measurement setup, extracting S-parameters, radiation patterns, realized gain, total radiation efficiency, and diversity parameters. Measurements were conducted with a vector network analyzer (VNA) and an anechoic chamber. During characterization, all nonactive ports were terminated with 50 Ω matched loads, and dummy elements were consistently terminated with 50 Ω loads. Owing to the antenna's symmetrical configuration, S-parameters were measured for ports 1, 3, 5, 7, 9, 11, 13, and 15.

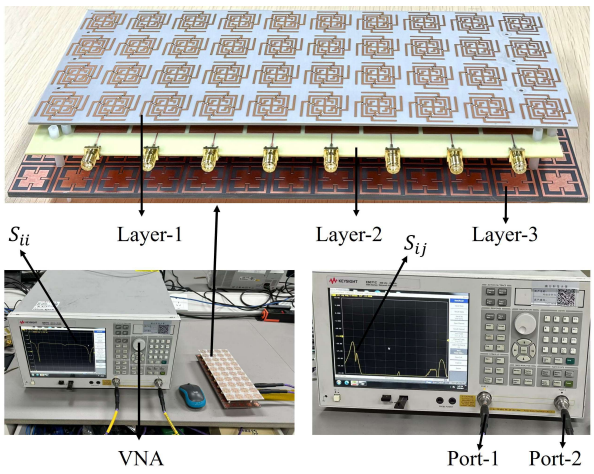

Fig. 26. Testing setup of the proposed CP mMIMO antenna using a VNA to determine its S-parameters.

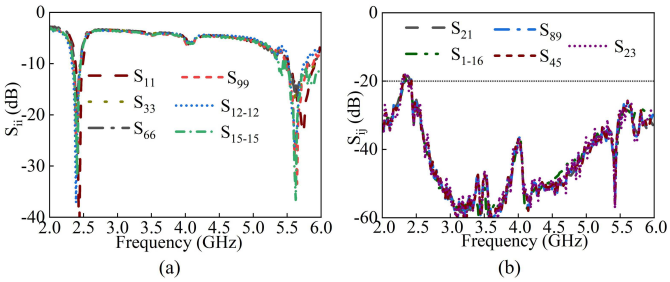

Fig. 27. Measured S-parameter of the proposed mMIMO antenna (a) S_{ii} and (b) S_{ij}.

The measured results in Fig. 27 confirm effective impedance matching and strong isolation across both operating bands. The measured −10 dB impedance bandwidth extends from 2.4–2.5 GHz in the lower band and 5.5–6 GHz in the upper band, which are in good agreement with the targeted ranges. Moreover, the measured MC consistently remains below −20 dB, validating excellent isolation between elements and confirming the suitability of the design for MIMO applications. Minor discrepancies between simulated and measured S-parameters are attributed to connector mismatches and measurement uncertainties, which are typical in practical implementations.

Fig. 28(a) and (b) illustrate the simulated and measured normalized radiation patterns at 2.45 and 5.85 GHz, respectively. In both cases, the antenna radiates broadside RHCP waves, which confirms consistent polarization behavior across the operating bands.

Fig. 29 compares simulated and measured results for gain, efficiency, and AR of the proposed mMIMO antenna. In Fig. 29(a), the measured gain reaches approximately 5.2 dBi at 2.45 GHz and 5.8 dBi at 5.85 GHz, closely matching

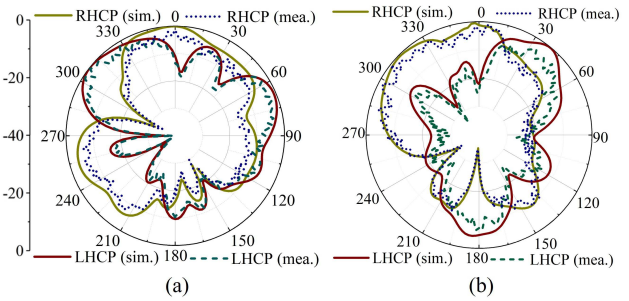

Fig. 28. Simulated and measured LHCP and RHCP radiation patterns at (a) 2.45 and (b) 5.85 GHz.

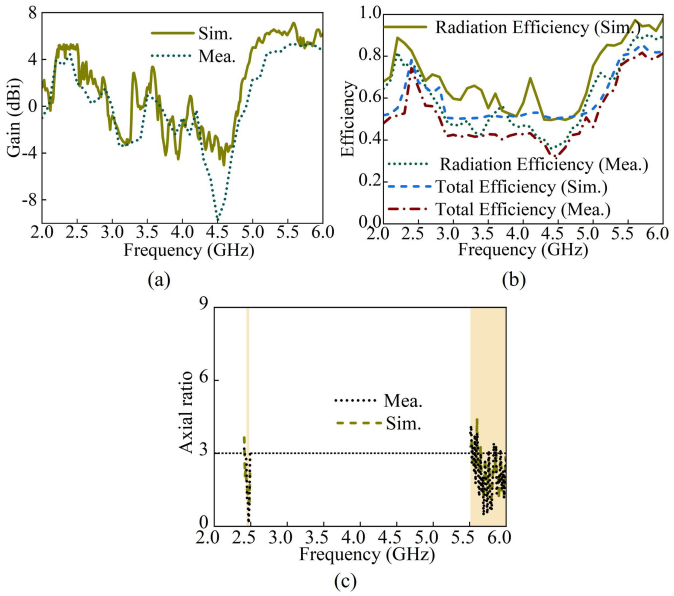

Fig. 29. Comparison between simulated and measured (a) gain, (b) radiation and total efficiency, and (c) AR.

the simulation. Fig. 29(b) presents the radiation and total efficiency, where both simulated and measured results exceed 78% across the operating bands. The measured values track the simulated trends, demonstrating reliable performance. The total efficiency accounts for ohmic losses, impedance mismatch, and feed network losses; thus, it is slightly lower than the radiation efficiency, which generally exceeds 90%. Finally, Fig. 29(c) shows the AR performance, where both simulated and measured curves remain below the 3 dB threshold across the operating bands, confirming a stable CP behavior.

F. MIMO Parameters

In a multielement system, relying solely on the scattering matrix to determine adequate bandwidth is insufficient. Therefore, additional performance indicators such as the envelope correlation coefficient (ECC), diversity gain (DG), mean effective gain (MEG), and channel capacity loss (CCL) must be considered [25]. As shown in Fig. 30(a), the proposed mMIMO antenna achieves an ECC below 0.002 at both operating frequencies when evaluated using far-field radiation patterns. Such low values indicate excellent isolation and

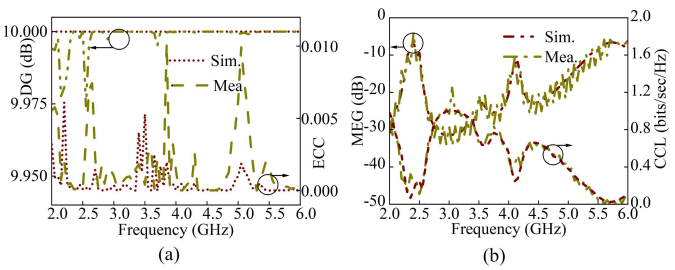

Fig. 30. Diversity analysis. (a) ECC and DG. (b) MEG and CCL.

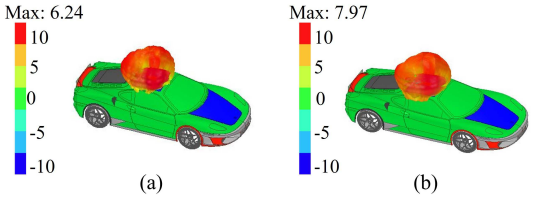

Fig. 31. 3-D gain of the proposed mMIMO antenna when it is mounted on roof top of a car at (a) 2.45 and (b) 5.85 GHz.

low correlation between elements. The corresponding DG is 9.99 dB at both bands, confirming strong diversity performance. Simulated and measured results exhibit only minor deviations within acceptable limits.

In addition, the MEG and CCL results are presented in Fig. 30(b). The measured MEG averages −5 and −8 dB for the 2.45 and 5.85 GHz bands, respectively. The CCL averages 0.2 bits/s/Hz in the lower band and 0.5 bits/s/Hz in the upper band. These values fall well below the commonly accepted 0.5 bits/s/Hz threshold, demonstrating efficient MIMO performance. Collectively, these results confirm that the proposed antenna exhibits low correlation, high DG, and minimal channel capacity degradation, ensuring reliable performance in practical MIMO deployments.

IV. Application Scenario

The 3-D gain radiation performance of the 16-port mMIMO antenna was further evaluated in an automotive scenario by mounting it on the rooftop of a metallic car body, as shown in Fig. 31. The vehicle body was modeled as a perfect electric conductor, while realistic material properties were assigned to the windscreen, seats, and mirrors. Using the car's CAD model in HFSS, both near-field and far-field characteristics were analyzed [33].

When mounted 10 mm above the roof surface [34], the antenna achieved peak gains of 6.24 dBi at 2.45 GHz and 7.97 dBi at 5.85 GHz. In free space, the corresponding gains were 5.23 and 5.83 dBi, respectively. The gain enhancement is attributed to constructive interference caused by image currents on the conductive rooftop acting as an extended ground plane.At the lower band, this configuration supports Wi-Fi communication, where omnidirectional coverage is critical for connectivity with in-vehicle and nearby devices, as shown in Fig. 31(a). The proposed mMIMO antenna also maintains an omnidirectional pattern at the upper band, as illustrated in Fig. 31(b).

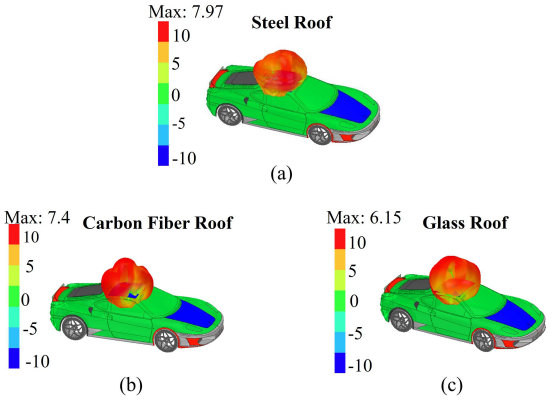

Fig. 32. Comparative analysis to determine the 3-D gain of the proposed antenna on different roof tops. (a) Steel roof, (b) carbon fiber, and (c) glass roof, respectively.

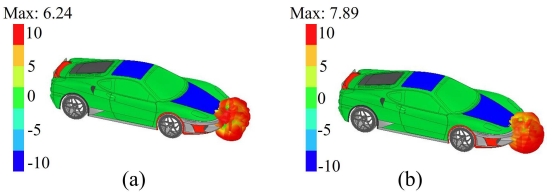

Fig. 33. 3-D gain of the proposed mMIMO antenna when mounted on a vehicle's front bumper at (a) 2.45 and (b) 5.85 GHz.

A comparative study was conducted to evaluate the influence of rooftop materials on radiation performance at 5.85 GHz, as shown in Fig. 32. When mounted on a steel roof, the gain reached 7.97 dBi [Fig. 32(a)], owing to strong image currents that reinforced forward radiation. On a carbon-fiber roof, the gain decreased to 7.4 dBi [Fig. 32(b)] because its partial conductivity weakens induced currents and causes partial absorption. The lowest gain, 6.15 dBi, was obtained on a glass roof [Fig. 32(c)], since the dielectric material does not support surface currents and permits radiation leakage through the roof.

In addition, the antenna performance was evaluated at different vehicle positions, including the front bumper and hood, to account for the varying ground plane conditions. The results indicate reliable operation across various positions with slight variations due to the underlying materials. Fig. 33 highlights the front bumper, a location particularly relevant for DSRC applications. Since the proposed antenna covers the DSRC band, it can be mounted on either the front or rear of the vehicle. These positions provide a clear line of sight, while their lower placement minimizes potential interference from the vehicle's structure or external obstructions. Moreover, as the bumper is primarily composed of metallic materials such as steel, it enhances the antenna's radiation through the formation of supportive surface currents, leading to improved gain performance. Consequently, the antenna achieves 6.24 dBi in the lower band and 7.89 dBi in the upper band, as illustrated in Fig. 33(a) and (b), respectively.

In addition, to assess the antenna's 3-D radiation performance with an infinite ground plane, it is on the hood, as

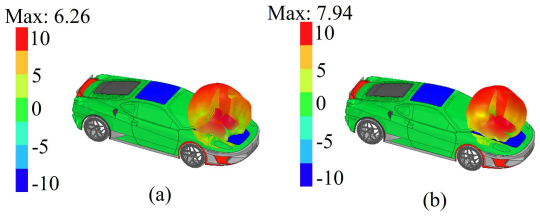

Fig. 34. 3-D gain of the proposed mMIMO antenna when mounted on a vehicle hood at (a) 2.45 and (b) 5.85 GHz.

shown in Fig. 34. This configuration achieves a high front-to-back ratio due to the infinite ground plane effect. The hood-mounted antenna exhibits performance nearly identical to that on the rooftop, making it suitable for desired applications. Overall, the far-field characteristics of the proposed mMIMO antenna array confirm its suitability for use in vehicles.

V. Comparison With Other Works

Table II provides a comparison between the proposed antenna and previously reported designs. Most of the earlier works, such as [6], [8], [11], [16], [17], [18], [19], and [23] support dual-band operation, while [9], [10], [35] focus on single-band performance. LP is still widely used in many of these designs, especially [6], [7], [8], [9], [10], [11], whereas CP becomes more common at higher frequencies [16], [19], [23], [36]. The proposed mMIMO antenna stands out by offering CP across two bands at relatively lower frequencies. When it comes to element spacing, few designs report compact edge-to-edge distances. Among those that do, only [6], [8], [10], [25] report relatively small spacing. Unlike previous designs, our antenna maintains a very compact structure with just 0.03 spacing between elements. Isolation is another crucial metric to consider in MIMO antennas. While some studies, such as [8] and [36], report high isolation exceeding 30 dB, they involve fewer elements. In our case, we achieve an isolation level of at least 22 dB within a 16-port array, providing strong decoupling even in a densely configured array. Many previous MIMO designs consist of only 2–6 ports, whereas our approach utilizes a full 16-port structure to enhance spatial diversity. Similarly, the achieved gain enhancements of 10.23 and 8.33 dBi across the two bands are also higher than those reported in earlier designs, such as [25] and [36], which show improvements of less than 6 dBi. In addition, it exhibits good axial ratio (AR) bandwidths (4.08% and 6.43%) as well as high radiation efficiency (90%), which highlights its effectiveness both in terms of polarization quality and overall performance. From the above discussion, it is evident that none of the existing studies have comprehensively addressed the overall performance of an antenna. Previous works have focused solely on individual aspects, such as mMIMO configuration, CP conversion, gain enhancement, or MC reduction; however, none have designed a multifunctional metamaterial-based antenna. In addition, for the first time, the performance of the antenna is investigated in different materials on the roof of cars, providing new information. Previous studies have

TABLE II
COMPARISON WITH PREVIOUS CP/LP MIMO AND SINGLE ANTENNAS

Ref.	f_0 (GHz)	Edge to Edge distance (λ_0)	No. of ports	Oper. Bands	Pol.	Isolation (dB)	Gain Enh. (dBi)	AR BW (%)	Rad. Effi. (%)
[6]	5.1	0	2	Dual-band	LP	$\geq$20	1,5	NA	80
[8]	3.7	0.034	2	Dual-band	LP	$\geq$25	2,1	NA	80
[9]	6.88	0.14	6	Single-band	LP	$\geq$22	4.05	NA	NA
[10]	9.2	0.0312	2	Single-band	LP	$\geq$13	1	NA	NA
[11]	0.825	0.12	4	Dual-band	LP	$\geq$25	NA	NA	90
[16]	18.5	NA	1	Dual-band	CP	NA	NA	29, 12	NA
[17]	18.7	NA	1	Dual-band	CP	NA	NA	34.3, 11.5	NA
[18]	22.5	NA	1	Dual-band	CP	NA	NA	5.56,3.97	NA
[19]	17.32	NA	1	Dual-band	CP	NA	NA	25, 16.4	NA
[23]	19.5	NA	1	Dual-band	CP	NA	NA	21, 6	NA
[25]	6.5	0.086	4	Dual-band	CP	$\geq$20	2, 3.5	6, 3.5	NA
[35]	3.75	NA	4	Single-band	CP	$\geq$20	NA	11	NA
[36]	3.37	NA	4	Dual-band	CP	$\geq$40	5.31, 4.3	2.7, 2.4	78
[This work]	5.4	0.03	16	Dual-band	CP	$\geq$22	10.23, 8.33	4.08, 6.43	90

Note: Pol. = Polarization, Oper. = Operating, Enh. = Enhancement, AR = Axial Ratio, BW = Bandwidth, Rad. Effi. = Radiation Efficiency

not thoroughly examined how roof material affects radiation characteristics.

VI. CONCLUSION

This article presents a high-gain, dual-band, circularly polarized 16-port mMIMO antenna designed and demonstrated for Wi-Fi and V2X communications. The design features a square patch with strategically placed slots for dual-frequency operation, achieving simulated and measured −10 dB bandwidths of 2.4–2.5 and 5.5–6 GHz, respectively. A novel multifunctional MLA incorporating lumped components was employed to reduce MC ($\leq$−22 dB) and achieved polarization conversion from linear to circular for the mMIMO elements. In addition, a CGAMC was integrated to enhance gain and radiation efficiency, delivering peak gains of 5.23 and 5.83 dBi in the lower and upper bands, respectively, with stable, symmetrical radiation patterns and radiation efficiency exceeding 90% across both bands. The design demonstrates excellent diversity performance, with an ECC below 0.001, a near-ideal DG of 9.99 dB, low CCL (0.15 bits/s/Hz), and a MEG of 7 dB. Similarly, the proposed mMIMO antenna was tested on different roof materials and various car mounting positions, with field evaluations on an automotive model further validating its suitability for V2X communication. These results confirm that the proposed dual-band CP-mMIMO antenna is an effective compact solution for MIMO communications in automotive applications, demonstrating excellent performance in both simulated and real-world scenarios.

REFERENCES

[1] A. Alghamdi, A. Basir, A. Iqbal, R. B. V. B. Simorangkir, M. Al-Hasan, and I. B. Mabrouk, "Compact antenna with broadband wireless biotelemetry for future leadless pacemakers," *IEEE Trans. Antennas Propag.*, vol. 73, no. 3, pp. 1870–1875, Mar. 2025.

[2] Z. Kuang, D. A. B. Miller, and O. D. Miller, "Bounds on the coupling strengths of communication channels and their information capacities," *IEEE Trans. Antennas Propag.*, vol. 73, no. 6, pp. 3959–3974, Jun. 2025.

[3] Y. Fang et al., "Resilience-oriented oscillation dampening for connected autonomous vehicle platoons," *IEEE Trans. Veh. Technol.*, vol. 73, no. 11, pp. 16024–16040, Nov. 2024.

[4] Y. Qin, M. Han, L. Zhang, C.-X. Mao, and H. Zhu, "A compact dual-band omnidirectional circularly polarized filtering antenna for UAV communications," *IEEE Trans. Veh. Technol.*, vol. 72, no. 12, pp. 16742–16747, Dec. 2023.

[5] A. Sultan, S. Jabeen, D. Fazal, and Q. U. Khan, "Dual-band dual-polarized MIMO design for vehicular applications," *AEU-Int. J. Electron. Commun.*, vol. 170, Oct. 2023, Art. no. 154772.

[6] W. Zhang, Y. Li, K. Wei, and Z. Zhang, "Dual-band decoupling for two back-to-back PIFAs," *IEEE Trans. Antennas Propag.*, vol. 71, no. 3, pp. 2802–2807, Mar. 2023.

[7] J. Deng, J. Li, L. Zhao, and L. Guo, "A dual-band inverted-F MIMO antenna with enhanced isolation for WLAN applications," *IEEE Antennas Wireless Propag. Lett.*, vol. 16, pp. 2270–2273, 2017.

[8] Z. Niu, H. Zhang, Q. Chen, and T. Zhong, "Isolation enhancement in closely coupled dual-band MIMO patch antennas," *IEEE Antennas Wireless Propag. Lett.*, vol. 18, pp. 1686–1690, 2019.

[9] P. Wang, J. Liu, G. Huang, Q. Wu, C. Zhou, and W. Wang, "Wideband gain enhancement of high-isolation and quasi-omnidirectional metamaterial MIMO antenna for vehicular radar," *IEEE Trans. Instrum. Meas.*, vol. 71, pp. 1–12, 2022.

[10] X. Chen, P. Wang, Y. Shao, and H. Jin, "Gradient relative permittivity superstrate for decoupling of two closely located dual-polarized slot antennas," *IEEE Trans. Antennas Propag.*, vol. 70, no. 4, pp. 3046–3051, Apr. 2022.

[11] Y. Zhu, Y. Chen, and S. Yang, "Decoupling and low-profile design of dual-band dual-polarized base station antennas using frequency-selective surface," *IEEE Trans. Antennas Propag.*, vol. 67, no. 8, pp. 5272–5281, Aug. 2019.

[12] L. Kong and X. Xu, "A compact dual-band dual-polarized microstrip antenna array for MIMO-SAR applications," *IEEE Trans. Antennas Propag.*, vol. 66, no. 5, pp. 2374–2380, May 2018.
[13] H. L. Zhu, S. W. Cheung, K. L. Chung, and T. I. Yuk, "Linear-to-circular polarization conversion using metasurface," *IEEE Trans. Antennas Propag.*, vol. 61, no. 9, pp. 4615–4623, Sep. 2013.
[14] C. Yang, G.-B. Wu, K. F. Chan, and C. H. Chan, "Linear-to-circular polarization conversion metasurface with broadband independent amplitude/phase control for sidelobe suppression," *IEEE Trans. Antennas Propag.*, vol. 71, no. 12, pp. 9944–9949, Dec. 2023.
[15] S. Yang, L. Liang, Z. Li, and W. Wang, "Ultrawideband MIMO circularly polarized cube antenna with characteristic mode analysis for wireless communication and sensing," *IEEE Internet Things J.*, vol. 11, no. 7, pp. 12192–12202, Apr. 2024.
[16] H. B. Wang and Y. J. Cheng, "Single-layer dual-band linear-to-circular polarization converter with wide axial ratio bandwidth and different polarization modes," *IEEE Trans. Antennas Propag.*, vol. 67, no. 6, pp. 4296–4301, Jun. 2019.
[17] H. B. Wang, Y. J. Cheng, and Z. N. Chen, "Dual-band miniaturized linear-to-circular metasurface polarization converter with wideband and wide-angle axial ratio," *IEEE Trans. Antennas Propag.*, vol. 69, no. 12, pp. 9021–9025, Dec. 2021.
[18] M. A. Sofi, K. Saurav, and S. K. Koul, "Frequency-selective surface-based compact single substrate layer dual-band transmission-type linear-to-circular polarization converter," *IEEE Trans. Microw. Theory Techn.*, vol. 68, no. 10, pp. 4138–4149, Oct. 2020.
[19] A. K. Fahad, C. Ruan, R. Nazir, T. U. Haq, and W. He, "Dual-band ultrathin meta-array for polarization conversion in Ku/Ka-band with broadband transmission," *IEEE Antennas Wireless Propag. Lett.*, vol. 19, pp. 856–860, 2020.
[20] R. Jie, H. Jing, S. Li, and Y. Xiao, "Dual-band circular polarizers based on a planar chiral metamaterial structure," *IEEE Antennas Wireless Propag. Lett.*, vol. 18, pp. 2587–2591, 2019.
[21] Y.-M. Cai et al., "Dual-band circularly polarized transmitarray with single linearly polarized feed," *IEEE Trans. Antennas Propag.*, vol. 68, no. 6, pp. 5015–5020, Jun. 2020.
[22] Z. Lin, R. Liu, X. Wang, H. Zheng, M. Wang, and E. Li, "Metasurface: Changing polarization from linear to circular for airborne antenna," *AEU-Int. J. Electron. Commun.*, vol. 116, Mar. 2020, Art. no. 153086.
[23] M. Del Mastro, M. Ettorre, and A. Grbic, "Dual-band, orthogonally-polarized LP-to-CP converter for SatCom applications," *IEEE Trans. Antennas Propag.*, vol. 68, no. 9, pp. 6764–6776, Sep. 2020.
[24] D. Chen et al., "A novel wideband compact circularly-polarized metasurface antenna for modern vehicular communication systems," *Microw. Opt. Technol. Lett.*, vol. 66, no. 2, pp. 920–926, Feb. 2024.
[25] A. Khan, Y. He, and Z. N. Chen, "A dual-band quad-port circularly polarized MIMO antenna based on a modified jerusalem-cross absorber for wireless communication systems," *IEEE Trans. Antennas Propag.*, vol. 72, no. 1, pp. 310–322, Jan. 2024.
[26] K. Paramayudha, S. J. Chen, W. Withayachumnankul, and C. Fumeaux, "Frequency-reconfigurable circularly polarized omnidirectional antenna," *IEEE Trans. Antennas Propag.*, vol. 70, no. 8, pp. 7205–7210, Aug. 2022.
[27] X. Hu, S. Yan, J. Zhang, V. Volski, and G. A. E. Vandenbosch, "Omni-directional circularly polarized button antenna for 5 GHz WBAN applications," *IEEE Trans. Antennas Propag.*, vol. 69, no. 8, pp. 5054–5059, Aug. 2021.
[28] Y. M. Pan, S. Y. Zheng, and W. Li, "Dual-band and dual-sense omnidirectional circularly polarized antenna," *IEEE Antennas Wireless Propag. Lett.*, vol. 13, pp. 706–709, 2014.
[29] L. Ge, S. Gao, Y. Li, W. Qin, and J. Wang, "A low-profile dual-band antenna with different polarization and radiation properties over two bands for vehicular communications," *IEEE Trans. Veh. Technol.*, vol. 68, no. 1, pp. 1004–1008, Jan. 2019.
[30] W. Cao, A. Liu, B. Zhang, T. Yu, and Z. Qian, "Dual-band spiral patch-slot antenna with omnidirectional CP and unidirectional CP properties," *IEEE Trans. Antennas Propag.*, vol. 61, no. 4, pp. 2286–2289, Apr. 2013.
[31] Y. Liu, X. Li, L. Yang, and Y. Liu, "A dual-polarized dual-band antenna with omni-directional radiation patterns," *IEEE Trans. Antennas Propag.*, vol. 65, no. 8, pp. 4259–4262, Aug. 2017.
[32] C. Guo, R. Yang, and W. Zhang, "Compact omnidirectional circularly polarized antenna loaded with complementary V-shaped slits," *IEEE Antennas Wireless Propag. Lett.*, vol. 17, pp. 1593–1597, 2018.
[33] S. Islam, H. Kim, T. D. Nguyen, S. Kim, and H. Yoo, "Reconfigurable mmWave planar phased array featuring wide elevation and full azimuth spatial coverage for 5G vehicular application," *IEEE Access*, vol. 13, pp. 8740–8752, 2025.
[34] J.-K. Che, C.-C. Chen, and J. F. Locke, "A compact four-channel MIMO 5G sub-6 GHz/LTE/WLAN/V2X antenna design for modern vehicles," *IEEE Trans. Antennas Propag.*, vol. 69, no. 11, pp. 7290–7297, Nov. 2021.
[35] C. Mao, M. Khalily, R. Tafazolli, and A. Kishk, "Wideband dual circularly polarized helical antenna with reduced mutual coupling for MIMO applications," *IEEE Trans. Antennas Propag.*, vol. 72, no. 4, pp. 3766–3771, Apr. 2024.
[36] P. Wang, J. Liu, C. Zhou, B. Yin, and W. Wang, "Dual-band dual-circularly polarized Fabry–Pérot cavity MIMO antenna using CMM-based polarization converter and MMA for vehicular satellite communications," *IEEE Trans. Veh. Technol.*, vol. 72, no. 7, pp. 8846–8857, Jul. 2023.

Asif Khan (Member, IEEE) received the B.E. degree in telecommunication engineering from Hazara University, Mansehra, Pakistan, in 2018, the M.S. degree in electrical engineering from North China Electric Power University, Beijing, China, in 2021, and the Ph.D. degree in information and communication engineering from Shenzhen University, Shenzhen, China, in 2024.

He is currently a Post-Doctoral Fellow with the College of Engineering, Southern University of Science and Technology, Shenzhen. His research interests include terminal antennas, multiple-input multiple-output (MIMO) antennas, shared-radiator antennas, and meta-antennas.

Qingsha S. Cheng (Senior Member, IEEE) received the B.Eng. and M.Eng. degrees from Chongqing University, Chongqing, China, in 1995 and 1998, respectively, and the Ph.D. degree from McMaster University, Hamilton, ON, Canada, in 2004.

In 1998, he joined the Department of Computer Science and Technology, Peking University, Beijing, China. In 2004, he became a Post-Doctoral Fellow and in 2007, a Research Engineer with the Department of Electrical and Computer Engineering, McMaster University. In 2014, he joined the Department of Electrical and Electronic Engineering, Southern University of Science and Technology (SUSTech), Shenzhen, China, where he is currently an Associate Professor. He has authored or co-authored more than 200 publications, including technical book chapters, refereed international technical journals, refereed international conference proceedings, and international workshops. His current research interests include AI-assisted and physics-driven smart modeling and optimization of microwave components and antennas, surrogate modeling and optimization, space mapping, multiobjective optimization, and neural networks.

Muhammad Zada (Member, IEEE) received the B.Sc. degree in telecommunication engineering from the University of Engineering and Technology, Peshawar, Pakistan, in 2015, and the integrated M.S./Ph.D. degree in electronic engineering from Hanyang University, Seoul, South Korea, in 2023.

He served as a Post-Doctoral Researcher at Hanyang University and later joined Shenzhen University, Shenzhen, China, as a Post-Doctoral Fellow. Currently, he is a Post-Doctoral Fellow with ETH Zürich, Zürich, Switzerland. He has authored numerous peer-reviewed journals and conference papers. His current research interests encompass functional materials for electromagnetics, including dielectric and conductive composites for stretchable and wearable electronics, strain-adaptive antennas, passive wireless sensing, energy harvesting, and implantable and textile-integrated systems for biomedical and human–machine interface applications.

Dr. Zada received the Best Student Paper Competition Award from the Korean Institute of Electromagnetic Engineering and Science (KIEES) in 2018 and the Best Ph.D. Thesis Award from Hanyang University. In 2024 and 2025, he was recognized among the world's top 2% scientists in the field of information and communication technologies. He serves as a reviewer for leading international publishers, including IEEE, Elsevier, Wiley, Nature Portfolio, and MDPI.

Zhonghe Zhang (Member, IEEE) was born in Jinzhong, Shanxi, China, in 1995. He received the B.S. and M.E. degrees from North University of China, Taiyuan, China, in 2018 and 2021, respectively, and the Ph.D. degree from the College of Electronics and Information Engineering, Shenzhen University, Shenzhen, China, in 2024.

He is currently a Post-Doctoral Researcher with Shenzhen University. His current research interests include millimeter wave antennas and arrays, reconfigurable antennas and arrays, and multibeam antennas and arrays.

Yejun He (Senior Member, IEEE) received the Ph.D. degree in information and communication engineering from the Huazhong University of Science and Technology (HUST), Wuhan, China, in 2005.

From 2005 to 2006, he was a Research Associate at the Department of Electronic and Information Engineering, The Hong Kong Polytechnic University, Hong Kong. From 2006 to 2007, he was a Research Associate at the Department of Electronic Engineering, Faculty of Engineering, The Chinese University of Hong Kong, Hong Kong. In 2012, he joined the Department of Electrical and Computer Engineering, University of Waterloo, Waterloo, ON, Canada, as a Visiting Professor. From 2013 to 2015, he was an Advanced Visiting Scholar (Visiting Professor) at the School of Electrical and Computer Engineering, Georgia Institute of Technology, Atlanta, GA, USA. From 2023 to 2024, he was an Advanced Research Scholar (Visiting Professor) at the Department of Electrical and Computer Engineering, National University of Singapore, Singapore. Since 2006, he has been a Faculty Member with Shenzhen University, Shenzhen, China, where he is currently a Full Professor with the College of Electronics and Information Engineering, the Director of Sino-British Antennas and Propagation Joint Laboratory of Ministry of Science and Technology (MOST), the Director of Guangdong Engineering Research Center of Base Station Antennas and Propagation, and the Director of the Shenzhen Key Laboratory of Antennas and Propagation. He was selected as an Expert with Special Government Allowance from the State Council in China, and a Leading Talent in the "Guangdong Special Support Program" in 2024. He was promoted to the Shenzhen "Pengcheng Scholar" Distinguished Professor in 2020. He has authored or co-authored more than 350 refereed journals and conference papers and seven books. He holds more than 30 patents. His research interests include wireless communications, antennas, and radio frequency.

Dr. He is a fellow of the IET and the China Institute of Communications (CIC). He was a recipient of the Shenzhen Overseas High-Caliber Personnel Level B (Peacock Plan Award B) and the Shenzhen High-Level Professional Talent (Local Leading Talent). He received the Second Prize of Shenzhen Science and Technology Progress Award in 2017, the Third Prize of Guangdong Provincial Science and Technology Progress Award in 2018, the Second Prize of Guangdong Provincial Science and Technology Progress Award in 2023, and the Tenth Guangdong Provincial Patent Excellence Award in 2023. He is currently the Chair of the IEEE Antennas and Propagation Society-Shenzhen Chapter and obtained the 2022 IEEE APS Outstanding Chapter Award. He has served as a Technical Program Committee Member or a Session Chair for various conferences, including the IEEE Global Telecommunications Conference (GLOBECOM), the IEEE International Conference on Communications (ICC), the IEEE Wireless Communication Networking Conference (WCNC), and the IEEE Vehicular Technology Conference (VTC). He served as the TPC Chair for IEEE ComComAp 2021 and the General Chair for IEEE ComComAp 2019. He was selected as a Board Member of the IEEE Wireless and Optical Communications Conference (WOCC). He served as the TPC Co-Chair for WOCC 2023/2022/2019/2015, APCAP 2023, UCMMT 2023, ACES-China 2023, NEMO 2020, and so on. He acted as the Publicity Chair of several international conferences, such as the IEEE PIMRC 2012. He has served as the Executive Chair of the 2024/2025 IEEE International Workshop on Radio Frequency and Antenna Technologies. He is the Principal Investigator for over 40 current or finished research projects, including the National Natural Science Foundation of China, the Science and Technology Program of Guangdong Province, and the Science and Technology Program of Shenzhen City. He has served as a reviewer for various journals, such as IEEE TRANSACTIONS ON VEHICULAR TECHNOLOGY, IEEE TRANSACTIONS ON COMMUNICATIONS, IEEE TRANSACTIONS ON INDUSTRIAL ELECTRONICS, IEEE TRANSACTIONS ON ANTENNAS AND PROPAGATION, IEEE WIRELESS COMMUNICATIONS, IEEE COMMUNICATIONS LETTERS, the *International Journal of Communication Systems*, and *Wireless Personal Communications*. He is serving as an Associate Editor for IEEE TRANSACTIONS ON VEHICULAR TECHNOLOGY, IEEE TRANSACTIONS ON ANTENNAS AND PROPAGATION, IEEE TRANSACTIONS ON MOBILE COMPUTING, IEEE ANTENNAS AND WIRELESS PROPAGATION LETTERS, *IEEE Antennas and Propagation Magazine*, *International Journal of Communication Systems*, *China Communications*, and *ZTE Communications*.

Qingfeng Zhang (Senior Member, IEEE) received the B.S. degree in electronics and information engineering from the University of Science and Technology of China (USTC), Hefei, China, in 2007, and the Ph.D. degree from Nanyang Technological University, Singapore, in 2011.

From June 2011 to December 2013, he was a Post-Doctoral Fellow at Polytechnique Montreal, Montreal, QC, Canada. Since December 2013, he has been with Southern University of Science and Technology (SUSTech), Shenzhen, China, where he is currently a Full Professor with the Department of Electronics and Electrical Engineering. His research interests are primarily in emerging novel electromagnetic technologies, in which he has a special interest in dispersion engineering at microwave and millimeter-wave frequencies.

Dr. Zhang is a fellow of the Institution of Engineering and Technology (IET). He received the Young Scientist Award at the 2018 URSI-RASC and 2018 ACES, as well as the Best Paper Award at the 15th Global Symposium on Millimeter-Waves and Terahertz in 2024. He served as the Founding Co-Chair of the IEEE Antennas and Propagation Society Shenzhen Chapter, which received the Outstanding Chapter Award in 2022. He served as the Associate Editor of IEEE ANTENNAS AND WIRELESS PROPAGATION LETTERS and as a Technical Program Committee (TPC) Member for various international conferences. He is a Distinguished Lecturer of electromagnetic science.